Experiments in Fluids (2025) 66:140
https://doi.org/10.1007/s00348-025-04062-5

RESEARCH ARTICLE

A combined intensity and lifetime-based laser-induced fluorescence technique (i-τLIF) with dye-doped nanobeads tracer for dissolved oxygen imaging below the water surface

E. Murniati[1] · A. Philippe[2] · O. Eiff[1] · H. Herlina[1]

Received: 20 December 2024 / Revised: 22 April 2025 / Accepted: 19 May 2025 / Published online: 27 June 2025

Abstract

The interfacial transfer process of atmospheric gases, such as oxygen, in a turbulent flow environment is characterized by a very thin concentration boundary layer with a highly dynamic concentration distribution further below the water surface. In order to capture such small-scale details at high time and spatial resolutions, a combined intensity and lifetime-based laser-induced fluorescence technique (i-τLIF) is presented. The combined method allows to use the iLIF method to obtain concentration images, while concurrently, one or more in situ benchmark data points are obtained non-intrusively using the τLIF method, which enables the reconstruction of the absolute (intensity to concentration) iLIF calibration curve from the generally valid normalized iLIF calibration curve. An accurate prediction of the benchmark points is possible, provided their values lie in the lower range of the oxygen concentration. The performance of the combined i-τLIF system was assessed by conducting experiments of interfacial gas transfer promoted by evaporative surface cooling. It was shown that the system was able to reveal the temporal and spatial variations of the concentration boundary layer as well as the structural developments of the deep-sinking plumes and the small-scale plumes that tend to linger near the surface, which are typically found in evaporative-cooling-induced gas transfer. Quantitative validation tests, including a one-to-one comparison of the i-τLIF results with microsensor measurements, yielded very good agreement. The high spatial resolution of the system allowed direct quantification of instantaneous concentration profiles and, hence, the estimation of the instantaneous gas transfer velocity.

Graphic abstract

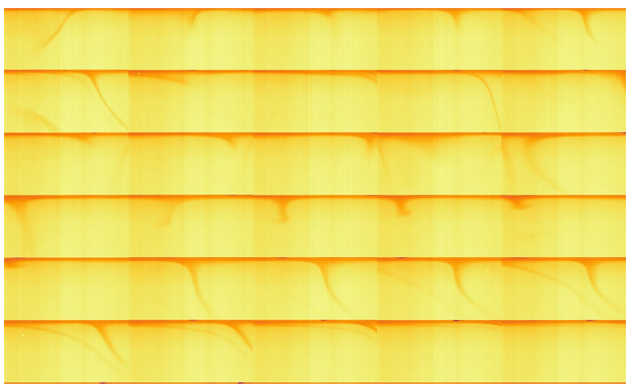

1 Introduction

The present work is motivated by the transfer process of atmospheric gases across the air–water interface. Important applications include absorption of carbon dioxide into the oceans and reaeration (oxygen absorption) into lakes and ponds. A fundamental understanding of the physical mechanisms that underlie such processes is of key importance, for example, to allow accurate predictions of the global atmospheric (including green-house) gas budget. Gas transfer across the water surface is controlled by the interaction

Extended author information available on the last page of the article

between molecular diffusion and the hydrodynamics near the interface, which is also strongly affected by the surface conditions. The task to resolve the gas concentration field near the water surface still poses a considerable challenge in both numerical simulations and laboratory experiments. The key difficulty lies in the fact that the transfer process of low to moderate soluble gases (such as oxygen, carbon dioxide and methane) is characterized by a very thin (gas-saturated) concentration boundary layer ($10-1000\ \mu$m) on the liquid side (Jähne and Haussecker 1998; Liss 1973). Recent applications of advanced numerical simulations (e.g., Wissink et al. 2017; Herlina and Wissink 2019; Herlina and Jirka 2008; Pinelli et al. 2022; Takagaki et al. 2016; Zhang et al. 2013) and experimental techniques (e.g., Kräuter et al. 2014; Jirka et al. 2010; Nagel et al. 2015) have provided improved insight into the problem. For the latter, optical dye-tracing techniques, such as laser-induced fluorescence (LIF), have become an important tool, as they allow non-intrusive visualization and quantification of small-scale dynamics of turbulent gas transfer processes (Crimaldi 2008; Rüttinger et al. 2018, and references therein). Below, the current status of LIF techniques for dissolved oxygen concentration measurements is briefly reviewed.

The basic components of an LIF system consists of a tracer, a light source (usually a pulsed laser) that excites the tracer and a camera that captures the luminescence (fluorescence or phosphorescence) emitted by the tracer. For dissolved oxygen concentration measurements, the LIF technique takes advantage of the luminescence quenching phenomenon of particular chemical compounds in the presence of oxygen. Such approach has been widely used for bioimaging in tissues and cellular microenvironment (e.g., Vaughan and Weber 1970; Wolfbeis 2015a, b; Digman et al. 2008; Fereidouni et al. 2011; Malacrida et al. 2021). The two most common oxygen indicators used in LIF techniques are pyrenebutyric acid (PBA) and some ruthenium complexes. The former have been employed mostly to characterize oxygen absorption through a flat air–water interface (e.g., Schladow et al. 2002; Herlina and Jirka 2004; Jirka et al. 2010), while the latter were mostly used to study mass transfer at a curved interface in the wake of individual bubble rising in a mixture of liquids (e.g., Roudet et al. 2017; Lebrun et al. 2021; Francois et al. 2011).

One characteristic of PBA-LIF systems is the relatively low signal-to-noise ratio (SNR), which mainly results from a combination of the following factors: (i) the dynamic range of the PBA fluorescence itself is relatively low (Münsterer 1996; Falkenroth et al. 2007), (ii) pulsed lasers inherently have a high shot-to-shot power fluctuation, and (iii) the expansion of a laser beam into a light sheet usually results in an inhomogeneous intensity distribution. The adverse effect of those factors becomes worse very near the water surface where high levels of quenching due to high oxygen concentrations are usually expected. Another drawback of using PBA is the need of photo-excitation in the UV region, which leads to the need of expensive optics, such as quartz glass and a high-energy pulsed UV laser, in order to obtain an adequate quantum yield. Ruthenium complexes, on the other hand, have a higher dynamic range than that of PBA (e.g., Castellano and Lakowicz 1998; Jimenez et al. 2014) and a relatively broad absorption band, located in the blue region ($400-480$ nm) of the visible spectrum (Wang and Wolfbeis 2014). However, their luminescence is highly temperature dependent, making Ruthenium complexes unsuitable for measurements in environments with large temperature variation (Santner et al. 2015; Rysgaard et al. 2008; Borisov and Klimant 2007).

Compared to PBA and ruthenium complexes, phosphorescent metalloporphyrins (e.g., PtTFPP and PtOEP, see Table 3 in appendix) provide a better sensitivity for luminescence detection (Papkovsky 1993, 2004; Wang and Wolfbeis 2014). They have in general higher quantum yields (≈ 0.4) and higher molar extinctions ($44-380$ mM), longer Stokes shifts (about 100 nm), longer luminescence lifetimes ($20-100\ \mu$s), and a better photostability (e.g., Lee and Okura 1997, cf. Table 3 in appendix). In addition, metallophorpyrins are generally less sensitive to temperature than ruthenium complexes (Wang and Wolfbeis 2014; Borisov and Klimant 2007). For instance, Friedl (2013) showed that the oxygen concentration estimate of ruthenium complexes deviates by $(c(T)-c(T_{ref}))/c(T_{ref}) = 3.1\%$ per Kelvin (where $c(T_{ref})$ is c at the reference temperature $T_{ref} = 20\,^{\circ}$C), while for PtOEP Papkovsky et al. (1993) obtained a deviation of 1.2%/K. The latter is in agreement with the results obtained in our experiments (cf. Fig. 17 in appendix). Consequently, metalloporphyrins have superseded PBA and ruthenium complexes (cf. Fig. 18 in appendix) and have become the most often used oxygen indicator in various sensor formats, such as fiber-optic sensors and planar film/optodes (Mosshammer et al. 2019; Santner et al. 2015; Wang and Wolfbeis 2014, and references therein).

In many cases, like in the case of interfacial gas transfer, the physical disturbance to the flow due to the presence of the sensor formats is undesirable. A solution to this is to coat/stain neutrally buoyant nanoparticles with metalloporphyrins (e.g., platinum tetrakis(pentafluorophenyl) phorpyrin and platinum octaetylphorpyrin) oxygen indicators. Incorporating fluorescent dyes into nanobeads for luminescence detection offers several advantages over dissolved dyes:

- Enhanced solubility: Nanobeads overcome water solubility limitations of certain dyes (e.g., PtOEP).
- Matrix isolation: Encapsulation in nanobeads prevents dye interactions with dissolved organic matter and surfaces, reducing measurement artifacts.

- Recyclability: Nanobeads facilitate easier removal and potential recycling of fluorescent markers through filtration, which is cost-prohibitive for dissolved dyes.

These stained nanoparticles can also be dispersed into the flow to serve as passive oxygen tracers for (non-intrusive) LIF measurements. Such an application of Pt-stained nanoparticles in an LIF system has been developed (Murniati et al. 2016) and used to study the dynamics of oxygen concentration distributions above the sediment-water interface in the presence of faunal activity (Murniati et al. 2017). This system, in contrast to the traditional intensity-based quantification method, is a lifetime-based method. The difference between these two methods is briefly described below.

In the traditional intensity-based LIF (iLIF) method, the change in intensity I is used as a measure for oxygen concentration c :

$$c(I) = \left(\frac{I_0}{I} - 1\right)/k_{SV}, \tag{1}$$

where I_0 is luminescent intensity in the absence of oxygen and k_{SV} is the Stern-Volmer (SV) constant (Vaughan and Weber 1970). Both k_{SV} and I_0 are determined via a calibration procedure. Accurate quantification of the oxygen concentration using the iLIF method requires both a uniform distribution of the tracer concentration and a uniform distribution of the excitation light intensity within the sampling area. In some cases, small spatial inhomogeneity in the dissolved oxygen tracer distribution can be neglected and systematic spatial inhomogeneity in the light sheet can be corrected via post-processing (e.g., Herlina and Jirka 2004). Even so, the luminescence intensity itself is sensitive to interference from other factors, such as the power drift of the excitation light, the turbidity of the sample, the background intensity, and photo-bleaching (Mosshammer et al. 2019). Consequently, it is difficult to obtain an absolute iLIF calibration curve that is valid for different experimental batches. However, it is possible to reconstruct an absolute iLIF calibration curve from the (generally valid) relative calibration curve. To this end, typically two in situ benchmark data points are required. This can be done, for example, by installing a sensor probe within the field of view (which is less favorable since the sensor introduces physical disturbances), or by assuming that the oxygen concentration takes on a constant value at/in a certain region inside the field of view (see, e.g., Herlina and Jirka 2004).

In contrast to the iLIF method, the lifetime-based LIF (τ LIF) method uses the locally measured luminescence lifetime (τ) to estimate the oxygen concentration:

$$c(\tau) = \left(\frac{\tau_0}{\tau} - 1\right)/k_{SV}, \tag{2}$$

where τ_0 is the luminescence lifetime in the absence of oxygen. The lifetime τ can be determined by evaluating the intensity decay of the luminescence after being excited by a short light pulse. Since the intensity I at time t can be described by the exponential decay law :

$$I(t) = I_{init} \cdot \exp^{(-t/\tau)}, \tag{3}$$

where I_{init} is the initial intensity at time $t = 0$ (Lakowicz 2010), the lifetime τ can be estimated by

$$\tau = \frac{t_2 - t_1}{\ln(I_1/I_2)}, \tag{4}$$

where I_1 and I_2 are the (accumulated) intensities measured within a short camera exposure time (Δ_{exp}) which starts at t_1 and t_2 after a short light excitation, respectively (de Grauw and Gerritsen 2001; Chan et al. 2001; Liebsch et al. 2000).

The major advantage of τLIF methods, as opposed to iLIF methods, is that it is not affected by (i) the tracer concentration, (ii) any spatial inhomogeneities in the excitation light intensity (Murniati et al. 2016), or (iii) any photo-bleaching (Mosshammer et al. 2019). Hence, a (generally valid) absolute lifetime calibration curve can be obtained (Murniati et al. 2016, 2017; Lo et al. 1996). A main drawback of any lifetime-based systems (e.g., Pt-based sensors and τLIF system) is their poor temporal resolution, which is a consequence of the relatively large integration time required for obtaining one (quasi-instantaneous) snapshot (cf. Sect. 3). For instance, the typical temporal resolution of 2D Pt-based sensors lies between $10 - 40$ s (Mosshammer et al. 2019; Santner et al. 2015). While the (non-intrusive) PtTFPP-τLIF system of Murniati et al. (2017) achieved a better temporal resolution of 2 s, for some applications this is still not short enough. Another disadvantage of the lifetime technique is that its sensitivity to variations in oxygen concentration at high oxygen levels is typically very low (Murniati et al. 2016).

To benefit from the advantages of both the τLIF and the iLIF methods without their respective limitations, we propose a novel approach complementing a Pt-based iLIF method with the τLIF method. This allows to use the iLIF method to obtain (quasi-instantaneous) oxygen concentration maps, while in situ benchmark data points (needed for the reconstruction of the absolute iLIF calibration curve) are obtained via the (non-intrusive) τLIF method. As a tracer, we employ PtOEP-stained nanobeads. The PtOEP luminescence is enhanced by the addition of macrolex yellow (MY) as a donor dye, while a time-gated 445-nm diode laser is used for the excitation source (see Sects. 2 and 3).

The performance of the new PtOEP i-τLIF system is assessed by conducting experiments of interfacial gas transfer driven by buoyant-convective flow. The measurements were conducted in a glass tank, which was placed inside a

climate chamber (cf. Fig. 1, further details of the experiments and i-τLIF components will be progressively discussed in the next sections). In the experiments, buoyancy-induced fluid motion is triggered by exposing warm water to cool air. Under such conditions, a thin (oxygen-saturated) cool thermal boundary layer forms. As the (slightly heavier) cool surface water tends to penetrate deep down into the bulk region, warmer water from below moves upward. As a result, oxygen-saturated surface water, in the form of thin falling plumes, is transported down and replaced by unsaturated bulk water from below. The i-τLIF system is employed to capture a small region (16.6 mm in width and 9 mm in height) immediately below the surface, with the aim of resolving the dynamics of these small scale oxygen concentration structures. It will be shown that the acquired sequences of oxygen concentration maps provided good qualitative insights into the near-surface gas transfer process. A one-to-one comparison between the obtained temporal oxygen concentration variations with that measured by an optical microsensor showed good agreement. Furthermore, the high spatial resolution allowed quantification of the instantaneous concentration profile below the surface. The present system can also be employed as a stand-alone τLIF mode, but at the expense of a significantly coarser temporal resolution of $\Delta W_\tau \sim 160$ ms as compared to $\Delta W_1 = 62.6$ ms with either the stand-alone iLIF or the combined i-τLIF approach. Examples will be given to demonstrate the pros and cons of the stand-alone τLIF versus the combined i-τLIF.

2 Synthesis and characteristics of nanobead oxygen tracers

The production of the PtOEP+MY nanobeads stock solution is described in the first part of this section. The chosen composition ratio of 1:3 between PtOEP and MY was based on the LIF measurements reported in Murniati et al. (2016). The applicability of the 1:3 composition was further evaluated by performing spectral measurements. The results are presented and analyzed in §2.2.

2.1 Synthesis

The PtOEP+MY nanobeads oxygen tracer were synthesized by core-staining poly-(1-vinylpyrrolidone-co-styrene) nanobeads (PVPS, Sigma-Aldrich GmbH, diameter 200 ± 50 nm) with PtOEP and macrolex yellow (MY). The latter serves as

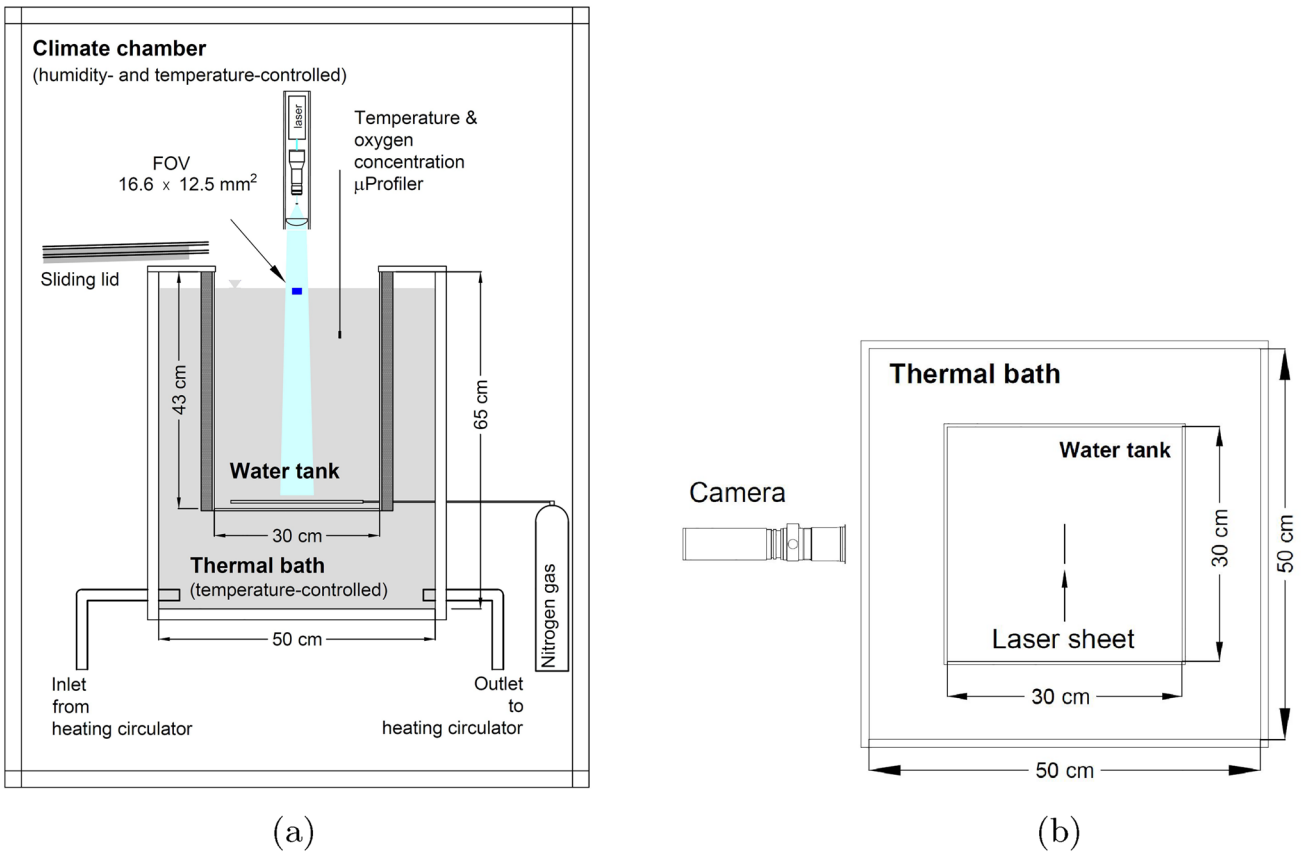

Fig. 1 Schematic of experimental setup: **a** cross-sectional view and **b** top-view

Table 1 Materials composition for synthesizing 100-ml stock solution oxygen tracer

Material	Specification	Amount
PVPS	density 1.04 g/ml	2.63 g
PtOEP	purity > 98%	5 mg
MY or C545T	purity > 98%	15 mg
THF	UV/IR Grade	300 ml
UP-Water	resistivity 18.2 MΩ cm	250 ml

a donor dye (cf. §2.2). The nanobeads were prepared using a procedure similar to Borisov et al. (2008). Some modifications to Borisov et al. (2008) procedure were necessary to reduce the re-precipitation of PtOEP and/or donor dyes, especially when scaling up the method to the gram scale. The materials with their specifications that are required to obtain a 100-ml final stock solution of the oxygen tracer are listed in Table 1.

The synthesizing procedure was as follows: In a 1-L round bottom glass flask, 2.63 g of PVPS nanobeads aqueous suspension (38% w/w emulsion) was diluted in 250 mL ultrapure water (UPW, Reinstwassersystem EASYpure II™, Werner, Germany) and 200 mL tetrahydrofuran (THF, Rotisolv, Carl-Roth GmbH) were added. This mixture was stirred vigorously using a magnetic stirrer for 20 min. The pH of the suspension was adjusted at this point with some drops of a concentrated NaOH solution (ROTIPURAN ≥ 32%, p.a., Carl-Roth GmbH) to ≈ 12.5. In a dropping funnel, 5 mg of PtOEP (Porphyrin Laboratories GmbH, Germany) and 15 mg of MY (Lanxess GmbH, Germany) or Coumarin 545T (Ossila BV, Netherland) were dissolved in 100 mL THF which were added dropwise (over ≈ 30 min) to the PVPS nanobeads suspension under continuous stirring. After 60-min stirring (including the addition), the THF and a part of the water was evaporated, a crucial step for the staining's success. Using a rotary evaporator at a rotation speed of 250 rpm, the suspension was heated up to 40 °C, the pressure was then adjusted to 340-220 mbar until around 200 mL of THF were evaporated. The recondensed THF was re-transferred to the round bottom flask containing the suspension. This suspension was stirred manually, sonicated in a sonication bath for around 10 s and was evaporated again following the above steps. We observed that this step visibly reduced the amount of re-precipitated dyes. The pressure was then slowly and carefully decreased to maintain a constant flow of solvent into the solvent collector until the pressure reached about 25 mbar. Maintaining this pressure, the remaining solvent was evaporated further until a bit less than 100 mL of water remained in the flask. The suspension

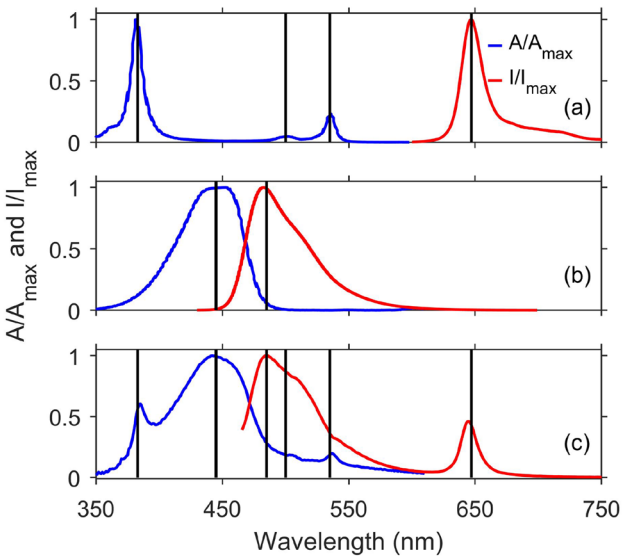

Fig. 2 **a** Measured absorption (*A*) and emission (*I*) spectra of PtOEP, **b** Macrolex Yellow and **c** the synthesized PtOEP+MY nanobeads. All measurements were performed at zero oxygen concentration

was then quantitatively transferred[1] to a 100-mL glass bottle. Note that the THF and most of the water, as far as the author can judge, were completely evaporated in the last step of the synthesis. Therefore, a very low concentration of THF in the final suspension was expected, such that possible changes to the water properties due to THF can be deemed negligible. It is also important to note that even though the nanobeads are perfectly dispersible in water, they are to some extent subject to agglomeration. To minimize the effect of the dye-tracer changing the water properties, the concentration of the dye-doped nanobeads was limited to the strict necessary. In addition, over time some hydrophobic dye can leach into the solution and may accumulate on the surface. To mitigate this, the usage of fresh stock solution is preferred and/or the particles could be freeze dried after the synthesis. The latter could prevent leaching of the dye during the storage time. The particles could then be suspended in the experimental medium shortly before they are needed.

2.2 Spectral analysis

The emission and absorption spectra of the tracer stock solutions were measured after each production using Perkin-Elmer LS55 and SPRecord 50, respectively.

Fig. 2 shows the results of the spectral measurements conducted for pure PtOEP, pure MY and the present synthesized PtOEP+MY stock solution. In line with the literature

[1] The transfer of a sample is from one container or vessel to another such that none is lost, a complete transfer.

(e.g., Lee and Okura 1997; Inglev et al. 2021), the spectra of PtOEP show strong absorption in the near UV range between 380 − 390 nm and two weaker peaks at 500 nm and 535 nm, while the emission peaks is located at 647 nm (cf. Fig. 2a).

The best option for pure PtOEP, therefore, would be excitation in the near UV region. However, the usage of (invisible) UV lasers is often unfavorable (see §1). Excitation in the visible range (> 400 nm), as can be seen in Fig. 2a, would lead to a significant loss in the absorption efficiency and in turn in a reduction in the emitted luminescence brightness. To mitigate this problem, researchers have utilized the so-called light harvesting method (Mayr et al. 2009). In such a method, the oxygen sensitive luminophore (e.g., PtOEP) is combined with an oxygen insensitive luminophore (e.g., MY, Coumarin). The latter is referred to as donor dye, and acts merely as an antenna by absorbing the excitation light and transferring its light energy to the oxygen sensitive luminophore, thereby increasing its luminescence intensity. A prerequisite for the aforementioned process is that the emission spectrum of the donor overlaps with the absorption spectrum of the oxygen sensitive luminophore. By comparing Fig. 2a and b, it can be seen that such an overlap exists between the emission of MY and absorption of PtOEP, in agreement with the spectra reported in, e.g., Larsen et al. (2011).

Figure 2c depicts the spectra of the present synthesized PtOEP+MY stock solution. The spectra clearly show the inherited characteristics passed from the individual components: one large absorption peak at 445 nm that stem from MY, and three smaller ones at 383, 500, 535 nm due to PtOEP, as well as a wide emission peak around 485 nm due to MY and a smaller one at 647 nm due to PtOEP. The measured PtOEP+MY spectra indicate that large amount of light absorption at 445 nm due to the MY-component would lead to a significant increase of energy transfer (in the overlap region) from the MY-component to the PtOEP-component and in turn enhances the PtOEP-component luminescence intensity at 647 nm (as opposed to direct excitation around 500 nm). This enhancement effect was confirmed for the present PtOEP+MY synthesis as shown in Fig. 3, where a significantly higher luminescence intensity was obtained at 445 nm excitation light as compared to excitations at 520 and 532 nm. Based on the results presented above, it was decided to use a blue laser with an output at 445 nm wavelength.

Furthermore, the oxygen quenchability, which is expressed by the ratio between the luminescence intensity at zero and at fully saturated oxygen concentration (Wang and Wolfbeis 2014) of the present PtOEP+MY synthesis, was analyzed (cf. Fig. 4). Based on the integrated area under the luminescence curves ($I_\lambda = \int_{\lambda=\lambda_f}^{\lambda=800} I \, \mathrm{d}\lambda$), the quenchability was found to increase from 1.6 to 1.8 when using long-pass filters with cutoffs at $\lambda_f = 550$ nm and $\lambda_f = 570$ nm, respectively. Thus, to block luminescence contributions that stem from the MY-component (cf. also Fig. 2), a long-pass filter with a cutoff at 570 nm was mounted in front of the camera.

As mentioned above, the 1:3 (w/w) composition ratio of PtOEP:MY was chosen based on the LIF results of Murniati et al. (2016). Here, for comparison, we also tested Coumarin (C545T) as an alternative to MY. For the same 1:3 (w/w) composition, no significant differences between PtOEP+MY and PtOEP+C545T were found (cf. Fig. 4). When changing the composition of PtOEP+C545T from 1:3 to 1:1, the luminescence intensity was found to reduce by half. A similar trend is expected when reducing the amount of MY (see Murniati et al. 2016). Note that a further increase of MY could result in self-quenching (Mayr et al. 2009) and thus a reduction in the luminescence brightness (Ma et al. 2016). The reason for using MY in this study was merely due to its lower price.

3 Optical setup of the i-τLIF system

The aim is to develop a system suitable for resolving quasi-instantaneous oxygen-saturated fluid transport driven by surface cooling. As mentioned earlier, such a transport process

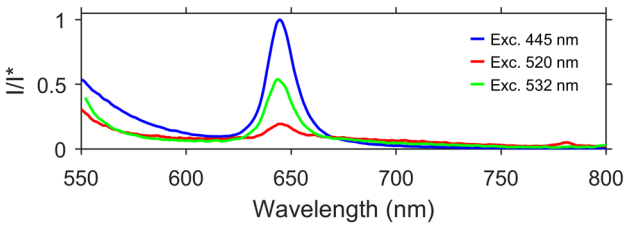

Fig. 3 Comparison of luminescence intensity of the present oxygen indicator (measured at zero oxygen concentration) excited by 445 nm wavelength, and by two most commonly used green lasers: 520 nm, and 532 nm

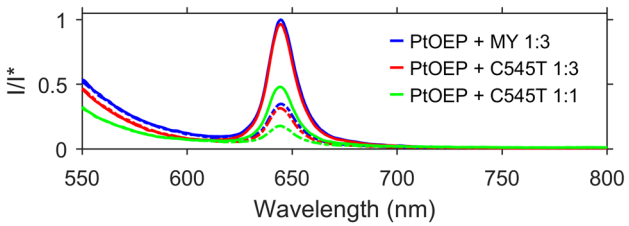

Fig. 4 Luminescence intensity of three enhanced-PtOEP variants excited by 445 nm at zero oxygen concentration (solid lines) and at 100%-air saturation (dashed-dotted lines). The intensities are normalized by I^*, which denotes the maximum intensity measured for PtOEP+MY 1:3

is marked by a very thin oxygen-saturated boundary layer and thin plumes of oxygen-saturated water further below the water surface. To capture the small scale dynamics of the oxygen concentration distribution, a spatial resolution of $< 50\ \mu$m and a recording interval of at most 250 ms are desired (Jirka et al. 2010). To achieve the required resolutions, the illumination and optics configuration were designed as follows.

As discussed in §2.2, a continuous 4-W diode laser with a wavelength of 445 nm (B445-4000 CM, Opt Lasers, Poland) was selected as illumination source. The laser beam had a cross-sectional area of 4.3×4.5 mm^2 at its exit point and was contracted using a 10 : 1 Galilean beam compressor (GBE10A, Thorlabs GmbH). A plano-concave cylindrical lens with focal length $f = -4$ mm expanded the contracted beam into a light sheet. To minimize the divergence of the light sheet, a 100-mm-wide plano-convex cylindrical lens with a 200 mm focal length was installed. With this setup, a laser sheet thickness of 0.5 mm was reached in the FOV with a total width of approximately 10 cm.

Image acquisitions were performed using a modulated charge-coupled device (CCD) camera (PCO.1600 MOD, PCO AG) with an effective pixel resolution of 1600×1200 pixel^2 and a pixel size of $7.5 \times 7.5\ \mu$ m^2.

The modulation function enables accumulation of up to 500000 exposures into a single image. In cases when the luminescence intensity obtained in one exposure is too weak (as is the case here), the aforementioned accumulation procedure is often used to enhance the signal-to-noise ratio (e.g., Holst et al. 1998). To resolve the small scale structures, a high-aperture f/2 macro lens with a focal length of 100 mm and magnification of 0.5× (Zeiss-Milvus 2/100 M, Zeiss AG) was used and combined with an extension tube of 52.5 mm length to increase the magnification to 0.72×. This setup also allowed the working distance from the camera lens and the field of view (FOV) to be large enough (about 25 cm) so that a thermal bath of 50 cm width could be used (the physical setup will be discussed in Sect. 5). With this setup, a FOV as small as 16.6 mm ×12.5 mm was obtained, yielding a spatial resolution of approximately 10-11 μm/pixel, which can be considered sufficient for resolving the dynamics of the near-surface oxygen concentration. The depth of field was about 0.4 mm. The camera was slightly tilted upward (2 °) to avoid obstructions caused by the meniscus and to facilitate water surface detection via reflection (cf. Fig. 6). As discussed in §2.2, to ensure that only the luminescence corresponding to the emission of the PtOEP-component is captured by the camera, a 570-nm long-pass filter was mounted on the camera lens.

The quasi-instantaneous iLIF image was acquired using multi-exposures, with the timing protocol shown in Fig. 5a. A single exposure cycle comprises

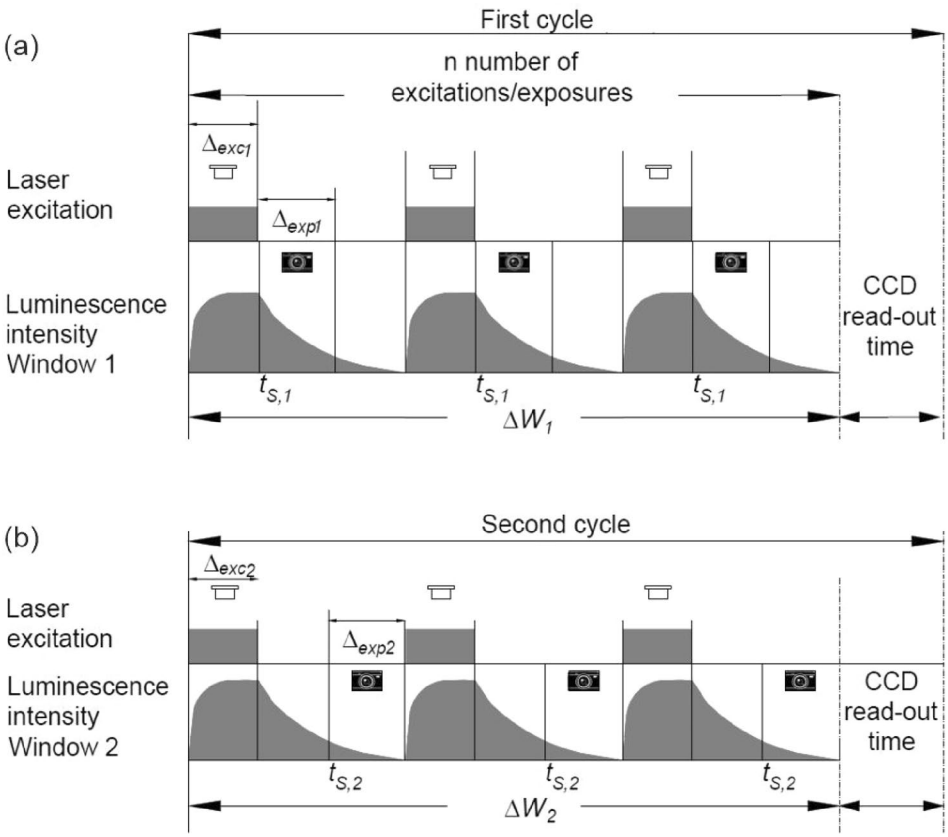

Fig. 5 Timing sequence to obtain one quasi-instantaneous intensity (a) and lifetime (a+b) image. n=1000, $\Delta_{exc} = 20\ \mu$s, $\Delta_{exp} = 22\ \mu$s, $\Delta t = t_{S,2} - t_{S,1} = 20\ \mu$s, CCD readout time = 34.6 ms

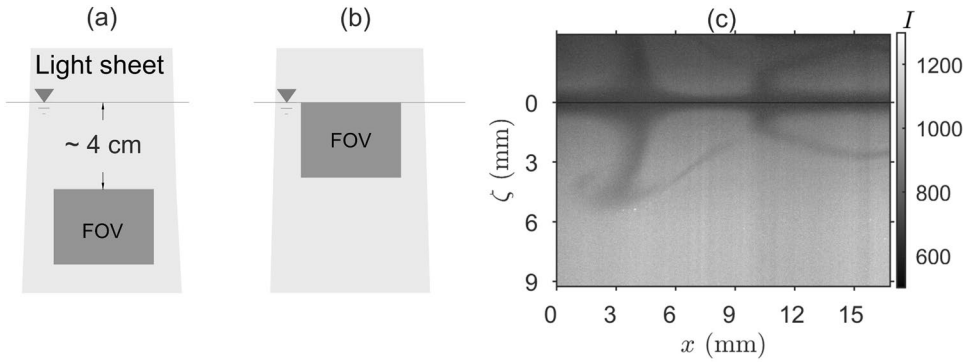

Fig. 6 Sketch of the bulk (**a**) and in situ (**b**) calibration setup and (c) a sample of near-surface intensity image obtained using 1000 multi-exposures, where the solid line at $\zeta = 0$ indicates the air–water interface. The image above the interface is a mirror image of the intensity image below the interface. The reflectional symmetry at $\zeta = 0$ was utilized to detect the location of the interface

$$\Delta S_1 = \Delta_{\mathrm{exc1}} + \delta_s + \Delta_{\mathrm{exp1}} + \delta_s + \Delta_1, \tag{5}$$

where $\Delta_{\mathrm{exc1}} = 20\,\mu$s is the laser excitation duration, $\Delta_{\mathrm{exp1}} = 22\,\mu$s is the camera exposure time during which the luminescence (due to phosphorescent reaction) emitted by the oxygen tracer is collected, $\delta_s = 0.3\,\mu$s is the safety margin before and after a camera exposure, and $\Delta_1 \geq 0\,\mu$s denotes the 'idle/waiting-time.'

Principally, Δ_1 can be omitted when employing the standalone iLIF measurement mode. Here, Δ_1= 20 μs was allocated/reserved to accommodate easy switching between iLIF and τLIF mode (cf. Fig. 5a and b). To achieve a sufficiently good signal-to-noise ratio, the complete single exposure cycle ΔS_1 was repeated $n = 1000$ times. Thus, the integration time required to obtain one intensity image—which also defines the temporal resolution of the intensity-based iLIF system—was $\Delta W_1 = n\Delta S_1 = 62.6$ ms. Adding the 34.6 ms CCD readout time, the sampling interval of consecutive (multi-exposure) iLIF images was $\Delta W_i = 97.2$ ms.

The lifetime-based concentration measurement (τLIF) requires information of luminescence intensities (I_1 and I_2 in Eq. 4), collected over two time periods (Δ_{exp1} and Δ_{exp2}) that are located inside the phosphorescence decay region. The timing protocol begins with one complete iLIF recording cycle (ΔW_1+CCD readout time, cf. Fig. 5a), followed by a second multi-exposure cycle ΔW_2 (cf. Fig. 5b). Note that while the first cycle Δ_{exp1} starts almost immediately after laser excitation has ended (at $t_{S,1} = 20.3\,\mu$s, where $t_S = 0$ marks the start of each laser excitation), the second cycle Δ_{exp2} begins at a significantly later time ($t_{S,2} = 40.3\,\mu$s), so that

$$\Delta S_2 = \Delta_{\mathrm{exc2}} + \Delta_2 + \delta_s + \Delta_{\mathrm{exp2}} + \delta_s, \tag{6}$$

where the time-slot $\Delta_2 = 20\,\mu$s overlaps with Δ_{exp1}. The aforementioned time delay ($t_{S,2} - t_{S,1}$) corresponds to the separation time ($t_2 - t_1$) in Eq. 4. As a result, the temporal resolution of the lifetime-based τLIF system was $\Delta W_\tau = \Delta W_1 + \mathrm{CCD\ readout} + \Delta W_2 = 159.8$ ms.

4 Calibration curves

4.1 Bulk and in situ calibration procedures

To generate the calibration curves, two different procedures (bulk and in situ) were evaluated. Both procedures involved measurements of luminescence intensities at several known (target) oxygen concentrations. During the bulk calibration data acquisition, it was ensured that the water in the bulk region of the tank was fully mixed yielding a homogeneous oxygen concentration distribution in the water column. To this end, the FOV was positioned within the upper bulk region, about 4 cm below the water surface (cf. Fig. 6a) and a fast-response fiber-optic oxygen sensor (PM-PSt7, Presens GmbH) was placed slightly below the FOV.

For the in situ calibration, the position of the FOV and the background oxygen concentration were set corresponding to the application experiment. Therefore, the FOV was such that it captured an area of about 9 mm below the water surface (see Fig. 6c). Inside the FOV, an orifice (inner dia. 3.6 mm) was placed to release sample water of known oxygen concentration into the test tank and the fiber-optic oxygen sensor was placed in front of the orifice to measure the oxygen concentration of the released water. The water temperature during the experiment was in the range of 21 ± 0.4 °C. Below it will be shown that i) the two curves differ significantly and ii) for the application case presented here, the in situ calibration procedure must be used.

Note that pre-processing steps were performed on all raw intensity images. These include (i) reduction of background random noise through averaging using a 5 × 5 pixels mean filter, and (ii) detection of the location of the water surface utilizing the reflectional symmetry at the interface (cf. Fig. 6c). In the present experiments, laser light attenuation associated to the Lambert-Beer effect was not detectable. In the analysis, data points within the first 80 μm below the interface were discarded to remove any doubts caused by, e.g., optical blurring effects and/or any unavoidable disturbances at the water surface, such as floating dust particles.

4.2 Intensity-based calibration curve

Figure 7a shows the obtained iLIF calibration curves, plotted in normalized I_o/I vs c/c_{sat} form. The data points represent the mean of a set of (at least 100) intensity (I) snapshots acquired at a respective (target) oxygen level. The error bars ($\pm\varepsilon$) indicate the uncertainty range of Io/I, which is based on two times the standard deviation ($\pm 2\sigma$) of the respective I dataset relative to its mean

$$\varepsilon = I_o/(I \pm 2\sigma). \tag{7}$$

It can be seen that the iLIF bulk dataset follows the Stern-Volmer relation (Eq. 1), where the normalized intensity I_o/I increases linearly with c/c_{sat}. The fitted slope was found to be $k_{SV} = 4.23$. Also included in Fig. 7a are curves of some commonly used indicators, such as PBA (Vaughan and Weber 1970), and ruthenium complexes $Ru[dpp(SO_3Na)_2]_3)Cl_2$ (Castellano and Lakowicz 1998) and $C_{36}H_{24}Cl_2N_6Ru.xH_2O$ (Jimenez et al. 2014). Compared to the aforementioned indicators, the quenching ratio

$$k_e = I_o/I - 1 \tag{8}$$

—which in the case of a linear relationship between I_0/I and c/c_{sat} is equal to k_{SV} - of the present iLIF system was found to be much larger, indicating its significantly higher sensitivity to oxygen, particularly in the lower oxygen concentration range (further discussed below).

While the bulk calibration dataset was obtained in an environment where the dissolved oxygen distribution was homogeneous in the entire water column, the condition during our application experiment was naturally inhomogeneous due to the interfacial gas transfer. This discrepancy may lead to false conversion of intensity to concentration. Indeed, this was proven to be the case: Conversion of the gas transfer intensity images by employing the bulk calibration curve resulted in unreasonable low values of concentration estimates as compared to the ground truth (oxygen probes) values. The above result suggests the need of an in situ calibration procedure for accurate oxygen concentration estimates.

Figure 7b depicts the obtained in situ calibration curve (ICC). It clearly shows a nonlinear trend, and thus Eq. 1 no longer holds. For such cases, the relation between intensity (I) and concentration (c) can be described by the modified SV equation by including a non-quenchable fraction of luminescence α (e.g., Frederiksen and Glud (2006)),

$$\frac{I_0}{I} = \left(\alpha + \frac{1-\alpha}{1+k\,c}\right)^{-1}, \tag{9a}$$

$$c = \frac{I_0 - I}{k\,(I - \alpha\, I_0)}. \tag{9b}$$

Here, $\alpha = 0.5$ and $k = 4.89$ were found to fit the data best. The quenching ratio was found to reduce from $k_e = 4.23$ in the bulk calibration curve (BCC) to $k_e = 0.68$ in the in situ calibration curve (ICC). Contrary to the implementation of the BCC (Fig. 7a), implementation of the ICC (Fig. 7b) to the gas transfer application experiments showed good agreement with the simultaneous ground truth (probe)

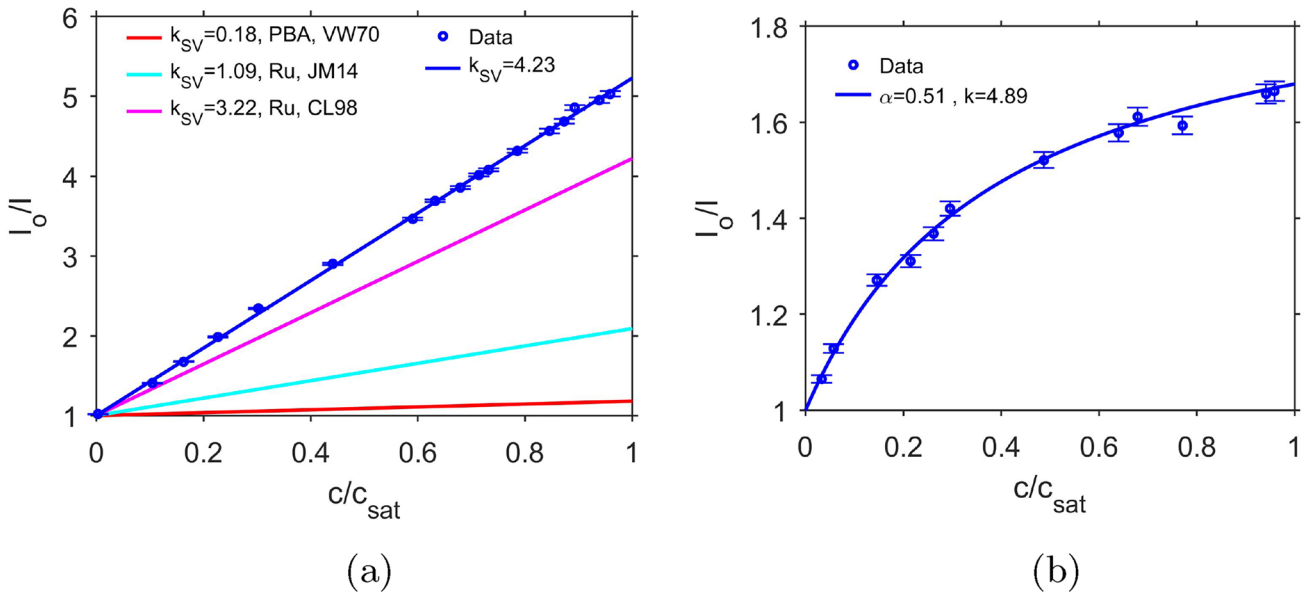

Fig. 7 iLIF calibration curves obtained **a** using the bulk procedure (homogeneous concentration distribution in the water column) and **b** employing the in situ procedure (non-homogeneous condition). Also included in (a) are SV curves of some common tracers used for LIF applications

measurements (cf. §5.3). The parameter α, according to Glud et al. (2016); Kühl and Polerecky (2008); Frederiksen and Glud (2006), is typically constant for a particular oxygen tracer and optical imaging system. The same was also observed in this study, where data points from repetitive calibration measurements collapsed on the same normalized curve.

The normalized uncertainty range (precision) of the concentration estimate at each oxygen level caused by random fluctuations in the measured intensity— which originate from a combination of random background noises, inconsistencies in the illumination intensity, and inhomogeneities in the tracer distributions is

$$\varepsilon_c = \pm\frac{\varepsilon}{k}, \tag{10}$$

where ε has been defined in Eq. 7 and k is the local slope in the ICC. As ε is inversely proportional to k, it is expected that the flattening of the ICC will lead to an overall higher uncertainty range in the in situ calibration as compared to the bulk calibration (cf. Fig. 7a and b). As can be seen in Fig. 8, the maximum ε_c of the ICC was found to be significantly larger as that of the BCC. It should be noted, however, that a reasonably low $\varepsilon_c \leq \pm 0.055$ was still achieved for the ICC.

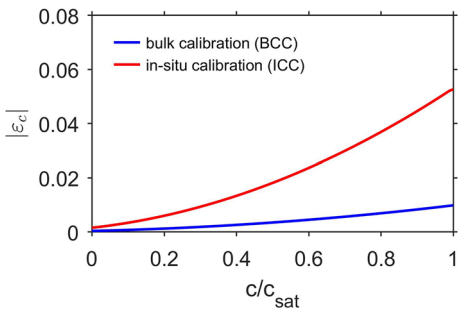

Fig. 8 Normalized uncertainty of the bulk (BCC) and in situ (ICC) iLIF calibrations

4.3 Lifetime-based calibration curve

The lifetime calibration curves (τ versus c/c_{sat}) are shown in Fig. 9, whereby τ was estimated using Eq. 4, with I_1 and I_2 taken from the datasets measured during the ICC series (blue symbols) and BCC series (red symbols). The two curves differ significantly. In the BCC series, the obtained lifetime ranged from $\tau_0 = 92\ \mu$s to $\tau_1 = 21.92\ \mu$s, in the ICC series τ ranged from 91 μs to 56.4 μs, with τ_0 and τ_1 measured at $c/c_{sat} = 0$ and $c/c_{sat} = 1$, respectively. The obtained $\tau_0 = 91 - 92\ \mu$s is in very good agreement with $\tau_0 = 89 - 90\ \mu$s reported in Murniati et al. (2016). The parameters for the fitted curves,

$$\tau = \tau_0\left(\alpha + \frac{1-\alpha}{1+k\,c}\right), \tag{11}$$

were $(\alpha, k) = (0.12, 6.25)$ and $(0.59, 13.91)$ for the bulk and in situ datasets, respectively. The corresponding precision of the concentration estimate as a function of the oxygen concentration level is shown in Fig. 9b. It can be seen that in the lower concentration range ($c/c_{sat} \leq 0.15$), a high precision of the lifetime measurement was achieved. This was also validated via repetitive experiments of simultaneous τ LIF and probe measurements. At higher concentration range, however, the precision, especially for the in situ calibration curve, deteriorates rapidly. Hence, reliable estimates with $\varepsilon_c \leq 0.05$ can only be achieved for $c/c_{sat} \leq 0.3$.

4.4 i-τLIF approach

The application of the normalized iLIF calibration curve requires information of at least one pair of intensity-concentration benchmark values. It should be noted that while the precision (uncertainty range ε_c) of the present system is

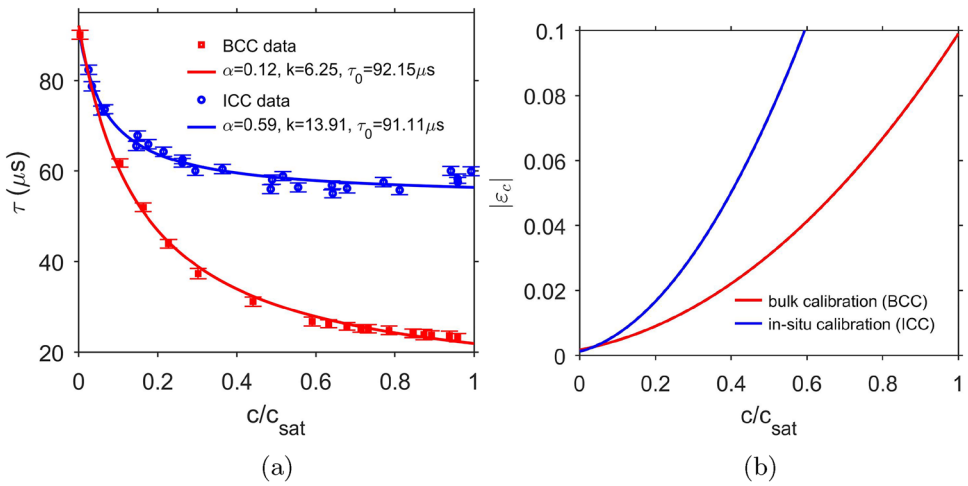

Fig. 9 **a** Bulk (BCC) and in situ (ICC) τLIF calibration curves and **b** their corresponding normalized uncertainties

affected by random fluctuations in the measured intensity (as discussed above), the accuracy of the present system depends highly on the correct determination of the aforementioned benchmark value. An ideal choice for the benchmark value would be the intensity I_0 measured at $c = 0$, which unfortunately is not always easy to obtain. Here, we take the data pair (I_b, c_b) located in the (on average) fully mixed region of the FOV as the benchmark value, with the consideration that the (typically very low) bulk concentration c_b can be determined locally and noninvasively using the τLIF approach with high accuracy, as shown above. Using the information of (I_b, c_b), I_0 can be determined by

$$I_0 = I_b\left(\alpha_+ \frac{1-\alpha}{1+k\,c_b}\right)^{-1} \tag{12}$$

and subsequently (9b) can be used to convert intensity images to oxygen concentration maps. For convenience, we denote the aforementioned conversion procedure as the i-τ LIF approach.

5 Application experiment

5.1 Experimental setup and procedure

As mentioned in §1, the i-τLIF system is evaluated by conducting experiments of (oxygen) gas transfer across the air–water interface driven by buoyant-convective instability. The buoyancy-induced fluid motion was triggered by exposing a body of warm water to cool, relatively dry air. The experiments were performed in a $30 \times 30 \times 43$ cm^3 glass tank (cf. Fig. 1). Except on the side of the tank where camera access is desired, all other side walls were insulated. To minimize any heat flux across the non insulated side wall, the test tank was placed inside a thermal bath ($50 \times 50 \times 65$ cm^3). The latter was connected via syphons to a second thermal bath, in which the water temperature was regulated by a heater (ME-26, Julabo GmbH, with a temperature stability of $\pm$ 0.01 °C). The overlying air temperature and humidity were controlled by an enclosed air-chamber regulator system. Note that the enclosed chamber was not designed as a cleanroom.[2] Thus, it was virtually impossible to maintain a perfectly clean water surface condition. Even though the water surface was cleaned by skimming / vacuuming prior to each experiment, some time after the surface was exposed to the ambient air, it was subject to airborne and surface particles.

The tank was equipped with an oxygen and temperature microprofiler. The oxygen sensor (PM-PSt7, Presens GmbH) has a tip diameter <50μm, an accuracy of $\pm$ 3% with a response time of $t_{90} \sim 0.6$ s and a maximum sampling frequency of 1 Hz. The thermistor (FP07, Amphenol GmbH) is a glass-bead negative temperature coefficient (NTC) thermistor with a tip diameter of 150 μm. It has an accuracy of $\pm$ 10 mK with response times in water and air of 7 ms and 100 ms, respectively. Both sensors were mounted on a frame and placed on a linear actuator (EAS4X, Oriental Motor GmbH). The shortest distance between measurement points was dictated by the highest sampling frequency of the sensors combined with the speed of the actuator. By setting the speed to 10 μm/s, the shortest distance achieved was 10 μm for oxygen concentration and 0.4 μm for temperature. The near-surface water temperature (T_s) was recorded using an infrared camera (VarioCAM HD head 880 S, Infratec GmbH, thermal resolution of 20 mK).

Before each experiment, the tank was thoroughly cleaned and filled with demineralized water. Afterward, 76.5 ml of PtOEP+MY stock solution was added (using a syringe with a 5 μm pore size filter to remove any coagulated nanoparticles present in the stock solution), resulting in a tracer concentration of 0.2% of the volume of the water in the tank. The surface tension was measured using a tensiometer (DCAT21, DataPhysics Instruments GmbH). The surface tension before and directly after adding the dye-doped nanobeads stock solution to fresh demineralized water was found to remain similar, i.e., 71.7 $\pm$ 0.1 mN/m and 70.6 $\pm$ 0.1 mN/m, respectively. The surface tension of water samples taken in situ was found to range between 57 and 69 mN/m depending on how long the water has been left in the tank. These reductions were mainly due to contamination from airborne and surface particles, such as dust that have accumulated on the water surface over time. To induce the gas transfer process, dissolved oxygen was purged out of the water via nitrogen-gas bubbling. The initial oxygen concentration was typically about 8–12%. Subsequently, to remove floating dust particles from the surface, the surface was cleaned using a vacuum/suction device. The final water depth after surface skimming was about 38.5 cm. Finally, the tank was closed to set the initial temperature condition (21 °C) and to obtain an initially quiescent water environment. The room temperature was set to 5 °C and the relative humidity (RH) was 60%. Measurements started after the lid was removed using an automatic removal system and t_0 was defined as the time when the water surface was fully exposed to the cool-ambient air.

Two types of experiments were conducted. In the first (BC1) experiment, two oxygen microsensor were placed within the FOV, allowing direct comparison between the results of the oxygen concentration estimates from the i-τLIF system with that measured by the (ground truth) microsensors. In the second (BC2) experiment, no probes were present inside the FOV, hence it can be seen as an actual application test case of the present non-intrusive measurement

[2] An enclosed space designed to control external contamination and environmental factors.

system. In addition, to estimate the transfer velocity K_L (also referred to as mass transfer coefficient or piston velocity), longtime concentration measurements in the deeper bulk region (about 4 cm below the bottom of the FOV) were performed.

The environmental conditions during the experiments are listed in Table 2. The Rayleigh number, $Ra = \alpha g(T_w - T_s)H^3/(\kappa\nu)$, was of the order of 2×10^9, where α is the coefficient of thermal expansion, g is the gravitational acceleration, κ is the thermal diffusivity, ν is the kinematic viscosity, and (T_w-T_s) is the water temperature difference between the bulk and the (near) surface, respectively. The latter was measured using the infrared camera. The total surface heat flux (q_t) is the sum of latent heat flux due to evaporation (q_e) and sensible heat flux due to the temperature difference across the water surface (q_s). The latent heat flux was estimated based on the evaporation rate, which was calculated based on the reduction of the water level over time (Soloviev and Lukas 2014):

$$q_e = L_v \rho_w E \tag{13}$$

where L_v is the latent heat of vaporization (2.45×10^6 J/kg at $T_w = 20$ °C), ρ_w is the density of water (998 kg/m^3 at $T_w = 20$ °C), and E is the evaporation rate (mm/day). The sensible heat flux (q_s) was calculated using the empirical approach from laboratory experiments (Jähne 1980):

$$q_s = w_w^a \ \rho_a \ c_{pa} \ (T_a - T_s), \tag{14}$$

where T_a, $\rho_a = 1.194$ kg/m^3, $c_{pa} = 1.007$ J/kgK are the temperature, the density and the specific heat of the overlying air, respectively, and w_w^a=0.776 cm/s is the transfer velocity of heat in the overlying air for no wind condition.

5.2 i-τLIF vs τLIF snapshots

Before proceeding with the results obtained using the proposed i-τLIF method, the limitations and advantages of the stand-alone τLIF system is described. As discussed in §3, application of the present system using the stand-alone τ LIF approach to obtain one (quasi-) instantaneous snapshot requires two integration times plus a readout time yielding an effective integration time of $\Delta W_\tau \sim 160$ ms, as compared to a single integration time of $\Delta W_1 = 62.6$ ms with the i-τLIF approach. Figure 10 shows a comparison between instantaneous oxygen concentration contour maps converted from intensity images using the i-τLIF approach (cf. §4.4) and the τLIF approach (equations (4) and (11)).

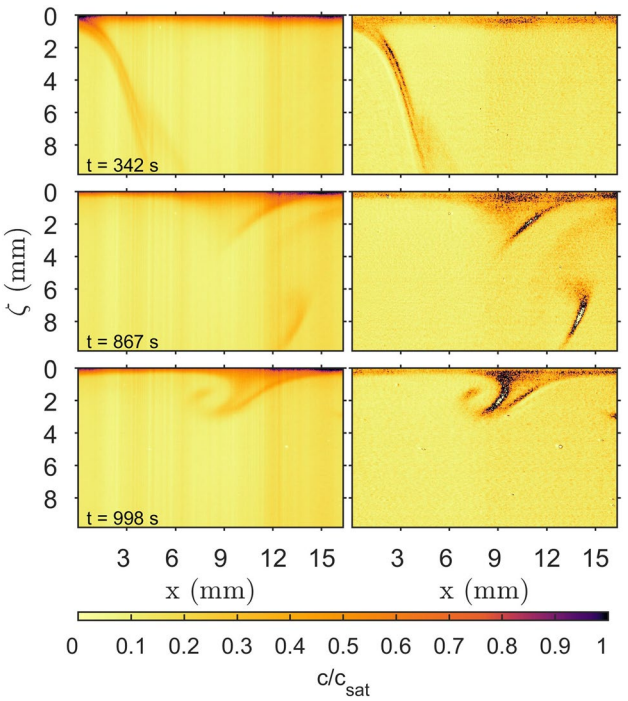

Fig. 10 Visualization of (quasi-)instantaneous oxygen concentration contour maps obtained using the combined i-τLIF approach (left-figures) and lifetime approach τLIF (right-figures)

It can be seen that, while the i-τLIF contour maps show reasonable oxygen concentration values virtually over the whole FOV, non-realistic concentration values (extending far beyond the 0 to 100% saturation range) occur in the τLIF contour maps, particularly in highly dynamic regions. This example clearly highlights the adverse effect of the large integration time ($\Delta W_\tau = 160$ ms) of the τLIF system on the oxygen concentration measurement. Note that accurate measurements require negligible concentration changes during an image-pair acquisition. Any non-negligible changes within this acquisition period will result in errors in the oxygen concentration estimations. In highly dynamic systems with short time scales, the errors may become very large as shown in the above example.

Table 2 Experimental conditions

Series	T_a °C	T_w °C	T_s °C	RH %	q_e W/m^2	q_s W/m^2	q_t W/m^2	
BC1	2	21.1	19	65	146	158	304	i-τLIF + two probes
BC2	4	21	18.6	58	244	135	379	i-τLIF

On the other hand, it can be seen that the inhomogeneities visible in the background bulk concentration in the i-τLIF snapshots (which are most likely caused by inhomogeneities in the incident laser intensity distribution, e.g., due to partial light blocking by dust particles at the interface) were not detected in the stand-alone τLIF contours. This demonstrates the advantage of τLIF, where concentration estimation is not affected by any spatial inhomogeneities in the light intensity. Since in the present application experiments of surface cooling-driven gas transfer, the concentration in most part of the bulk is virtually homogeneous, it is expected that τ LIF provides accurate concentration estimates in the bulk region, where the concentration is mostly homogeneous and low (see also Fig. 9).

It should be noted that another possible remedy for the poor temporal resolution of the τLIF system might be the use of two individual multi-exposure cameras for the acquisition of image-pairs for ΔW_1 and ΔW_2, respectively (see Fig 5). With this arrangement, the large CCD readout time between ΔW_1 and ΔW_2 can be eliminated, so that the integration time of one τLIF snapshot would be similar to the present i-τLIF approach.

5.3 Simultaneous i-τLIF and probe measurements

Below, the results of the BC1 validation experiment, with two oxygen microsensors placed within the FOV, are presented. Figure 11 shows the temporal variations in oxygen concentration measured by the i-τLIF system and one of the oxygen probes.

The probe was located about 0.23 mm below the water surface, while each i-τLIF data point represents the mean intensity of a 5×5 pixels (52×52 μm^2) interrogation area located in the proximity of the probe (about 0.16 mm to the left of the probe). As can be seen in Fig. 11, the i-τLIF data series shows very good agreement with the data series measured by the probe. Small discrepancies, including small time lags between the two signals, are mainly caused by the spatial gap between the interrogation area and the probe. In any case, both data series are of similar magnitudes and clearly exhibit the same trend in time: it can be seen that immediately after the water surface was fully exposed to the relatively dry and cool air ($t = 0$), c started to fluctuate energetically between $c/c_{sat} = 0.4$ to 0.9 over time. These fluctuations correspond to the upward movements of warm, unsaturated water parcels from the bulk to the water surface and the sinking of cold, gas-saturated water parcels from the surface to the bulk region. The local maxima and local minima correspond to events of low and high concentration gradients ($\partial c/\partial z$) at the surface, respectively. This is evidenced in Fig. 12, depicting i-τLIF profiles which correspond to the instances t_1 and t_2 in Fig. 11.

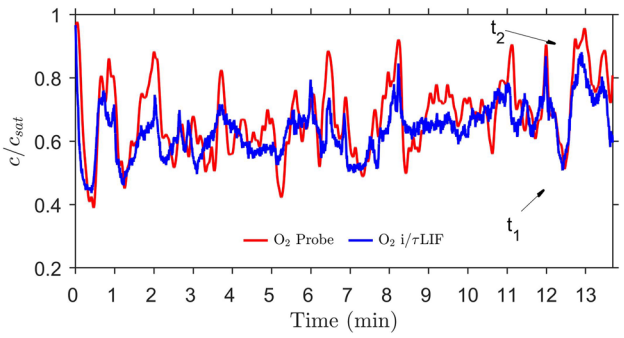

Fig. 11 Comparison of oxygen concentrations measured by an oxygen microsensor probe 0.23 mm below the surface and i-τLIF system 0.16 mm to the left of the probe

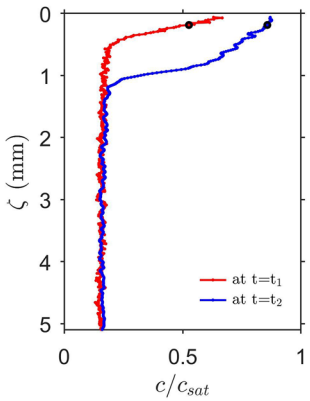

Fig. 12 Vertical oxygen profiles measured using the i-τLIF approach. The profiles correspond to the times t_1 and t_2 of the signal shown in Fig. 11, and the black circles indicate the corresponding data points

5.4 i-τLIF measurements

Evaporative surface cooling is characterized by unstable density gradients, and typically also by variations in surface tension due to local variations in surface temperature which generate Marangoni forces. Below the surface, a very thin thermal (oxygen-saturated) boundary layer forms, from which plumes of relatively cold (oxygen-saturated) water are released, while simultaneously being replaced by warm (unsaturated) bulk water from below. Figure 13 shows a sequence of oxygen concentration contour maps obtained from the BC2 experiment where no probes were present inside the FOV.

The images reveal the temporal and spatial variations of the (high oxygen-saturated) concentration boundary layer and also reveal fine structures corresponding to the development of oxygen plumes associated with the transport of oxygen from the water surface to the bulk water. In the first row of the sequence, a water parcel just below the water surface with a high concentration of oxygen can be seen to penetrate deep into the bulk region (deeper than the

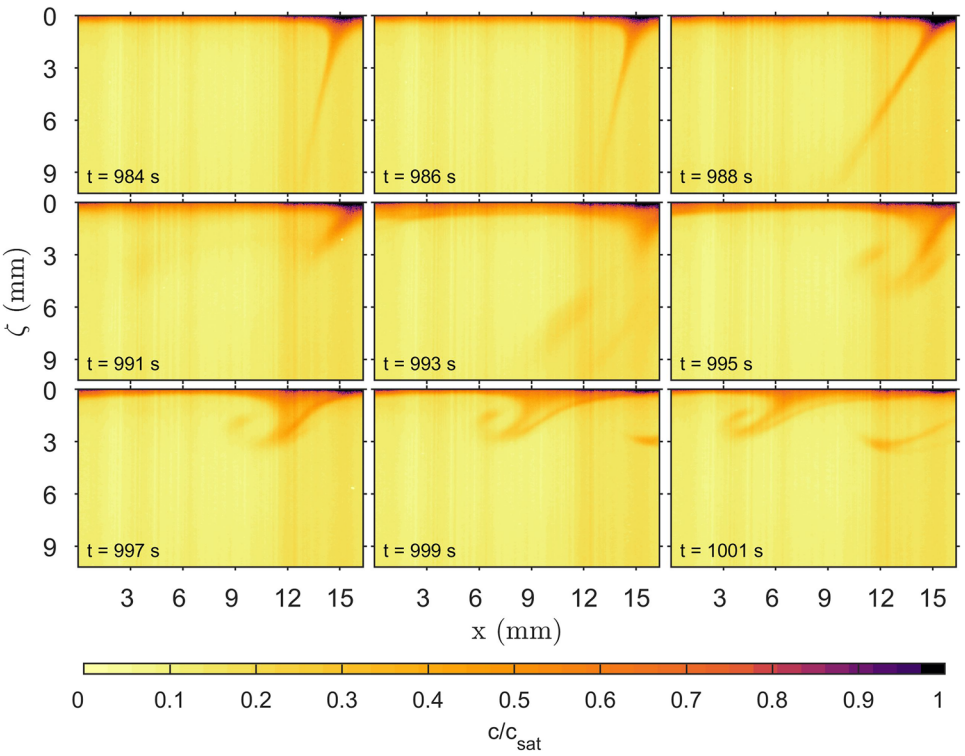

Fig. 13 Sequence of oxygen concentration images. The transfer of oxygen from the water surface to the bulk was promoted by surface cooling, which triggered buoyant-convective instability-driven flow motions. The recording time is indicated in each image, where $t = 0$ marks the time when the water surface was fully exposed to the cool and relatively dry ambient air

FOV). Such deep-penetrating structures associated with a buoyancy-driven instability were also reported in Jirka et al. (2010); Wissink and Herlina (2016). In the last row, a mushroom-like shape plume is advected while another plume appears on the right side, both continuing to be advected. These small-scale plumes tend to linger at the surface for a relatively long time and are likely associated to surface temperature gradients Marangoni-induced flow (see also Wissink and Herlina 2023).

A sample of a horizontally averaged concentration profile $\langle c \rangle_x$ taken from the BC2 dataset is shown in Fig.14a.

The fine resolution of 10.2 μm allowed quantification of the concentration gradient at the surface, and hence, the estimation of the instantaneous transfer velocity is defined as

$$k_L(t) = \left| \frac{D\partial\langle c\rangle_x/\partial\zeta}{c_{sat} - \langle c_b\rangle_x} \right|_{\zeta=0} = \frac{D}{\delta}, \tag{15}$$

where D is the molecular diffusion coefficient, $\langle c_b \rangle_x$ is the horizontally averaged bulk concentration and δ denotes the thickness of the concentration boundary layer. Figure 14b shows the resulting transfer velocity k_L as a function of time. The values are in very good agreement with the overall transfer velocity K_L, defined as

$$K_L = |K_2 H|, \tag{16}$$

where $H = 38.5$ cm is the depth of the water in the tank and K_2 is the reaeration rate. The latter was determined through longtime oxygen-probe measurements in the bulk region at approximately 4 cm below the FOV. Note that integration of the conservation of mass equation $\mathrm{d}c_b/\mathrm{d}t = K_2(c_{\mathrm{sat}} - c_{b,t})$ with an initial condition $(c_{\mathrm{sat}} - c_{b,t_o})$ at $t = t_o$ yields

$$\ln\left(\frac{c_{\mathrm{sat}} - c_{b,t}}{c_{\mathrm{sat}} - c_{b,t_o}}\right) = K_2(t - t_o). \tag{17}$$

The evolution of the bulk concentration c_b in form of (17) is shown in Fig. 15 and K_2 is given by the fitted slope of the curve.

As a final validation, the time and horizontally averaged concentration profile $\langle c \rangle_{x,t}$ was compared with profiles obtained from independent (but similar experimental conditions) microprofiling experiments. Two modes of vertical oxygen concentration and temperature μ-profiling were conducted: (1) discrete mode (P1), where at a certain position data were collected for 2 min before moving to the next location, and (2) continuous mode (P2), where the sensors were moved continuously and the interface was detected based on the distinct change of the raw value of the probe (phase-shift angle ϕ) upon entering the water. The duration of measurements were about 30 min and 15 min to complete a profile with a distance of 10 mm for case 1 and 2, respectively. The measured concentration profiles (P1 and P2 datasets) are

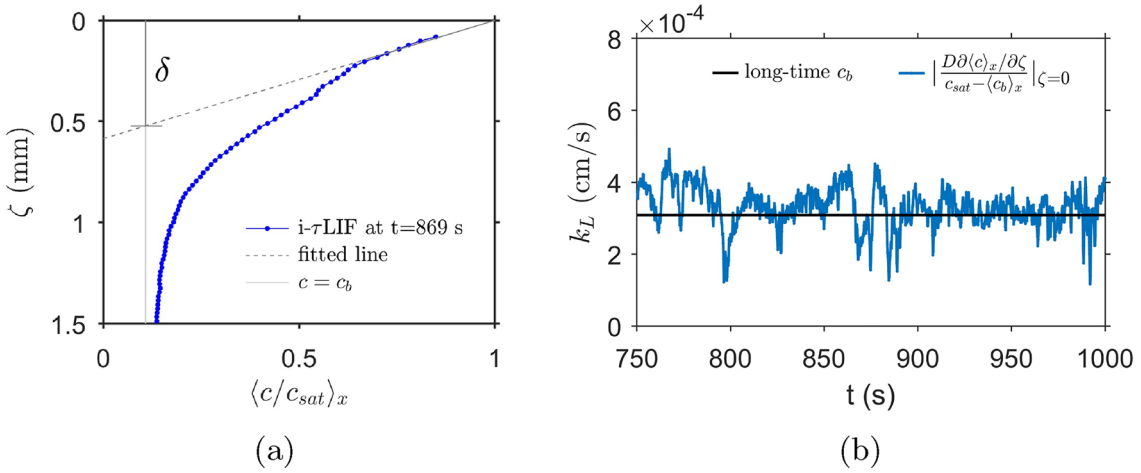

Fig. 14 **a** A zoomed-in view of $< c/c_{sat} >_x$ at $t = 869$ s, revealing the fine spatial resolution of the current system, which allows direct estimation of the concentration gradient at the surface ($\partial c/\partial\zeta|_{\zeta=0}$). In the plot, only every second data point is shown and δ denotes the boundary layer thickness, defined in (15). **b** Temporal variation of k_L determined using (15)

shown in Fig. 16 and compared with the time (over a duration of 250 s, 1275 images) and horizontally (over 8.125 mm, 800 pixels) averaged profiles obtained in BC2. All three datasets show very good agreement, illustrating the reliability of the i-τLIF approach.

6 Conclusions

To be able to capture the intricate and fast-evolving details of the gas transfer process across the air–water interface promoted by evaporative surface cooling, a combined intensity and lifetime-based laser-induced fluorescence technique (i-τLIF) was developed and systematically evaluated.

Accurate concentration measurements using traditional iLIF methods require a uniform distribution of both the tracer concentration and the excitation light. Since luminescence intensity is sensitive to interference from factors, such the power drift of the laser light, the turbidity of the sample, photo-bleaching, or the background intensity, it is very difficult to obtain a generally valid absolute iLIF calibration curve. The major advantage of τLIF systems as opposed to iLIF systems is that it is not affected by the tracer concentration, any inhomogeneities in the incident light intensity, or any photo-bleaching. The proposed combined i-τLIF system can also be used as a stand-alone τLIF system, but at the expense of of a significantly coarser temporal resolution of 160 ms as opposed to 62.6 ms with either the iLIF or i-τ LIF approach. The adverse effect of the large τLIF integration time on the oxygen concentration measurements can be seen in the occurrences of non-realistic concentration values,

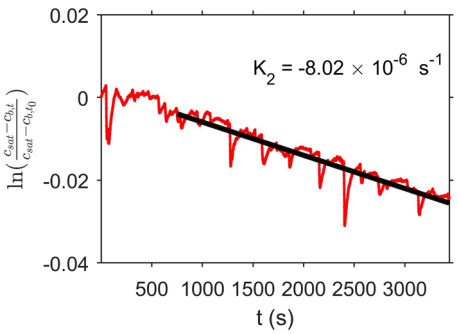

Fig. 15 Estimation of the reaeration rate K_2 based on the longtime bulk concentration measurements

especially in highly dynamic regions (cf. §5.2). Another drawback of a τLIF system is that its sensitivity is rather poor at high oxygen concentration levels (cf. Fig. 9b).

The coupling of the iLIF and τLIF methods, as proposed here, allows to benefit from the advantages of both methods without their respective limitations. In the proposed combined i-τLIF method, the iLIF approach is used to obtain instantaneous oxygen concentration maps, while in situ benchmark data points are measured using the τLIF method, which enables the reconstruction of the absolute (intensity to concentration) iLIF calibration curve from the generally valid normalized iLIF calibration curve. In the present application case, an accurate prediction of the benchmark points in the bulk region using the τLIF method is possible since the bulk oxygen concentrations lie in the lower range. The use of dye-doped PtOEP nanobead oxygen tracers in combination with a (445-nm) blue diode laser excitation, supported

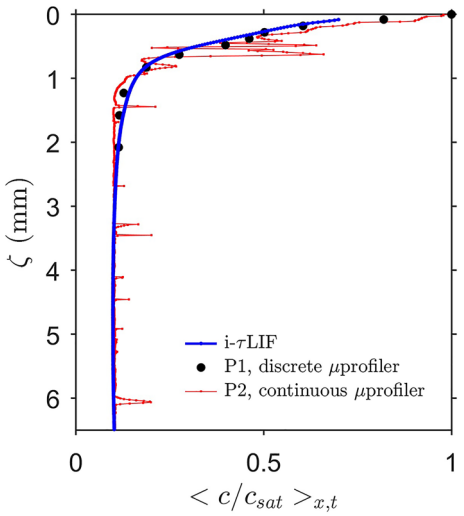

Fig. 16 A comparison of the mean oxygen concentration profile obtained using i-τLIF (BC2 dataset) with the profiles measured by the microprofiler (P1 and P2 datasets)

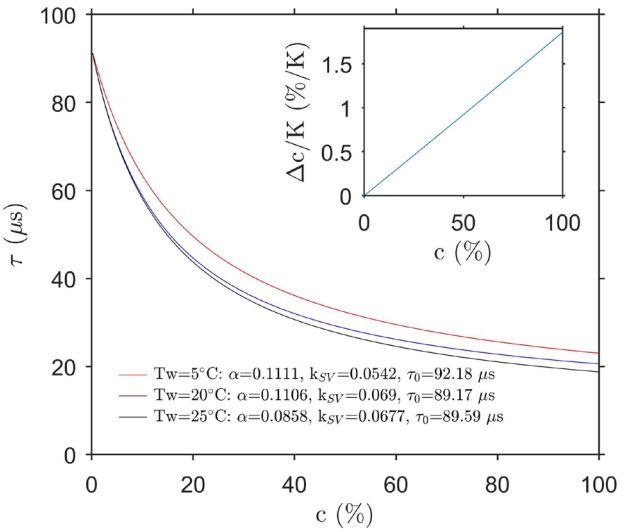

Fig. 17 Bulk lifetime calibration curves at three different water temperatures. The fitted parameters of the modified Stern-Volmer equation are shown in the legends. The inset shows the concentration deviation per Kelvin defined as $(c(T) - c(T_{ref}))/c(T_{ref})$, where $c(T_{ref})$ is c at the reference temperature $T_{ref} = 20\,^{\circ}\mathrm{C}$

by spectral analysis, significantly increased the luminescence intensity as compared to the 520 nm and 532 nm laser excitations. Two calibration procedures (bulk and in situ) were evaluated and it was found that implementation of the traditional bulk calibration curve resulted in unreasonable low concentration estimates, while application of the in situ calibration curve yielded reliable results. The spatial resolution achieved by the present system was 10.2 μm with a field of view (FOV) of approximately 9×16 mm^2. The high time and spatial resolutions of the new system enable not only the visualizations of the structure developments of deep-sinking oxygen-saturated plumes (shown, e.g., in Jirka et al. 2010), but also the small-scale oxygen-saturated plumes lingering near the surface that are typically found in evaporative-cooling promoted mass transfer (see, e.g., Wissink and Herlina 2023). Quantitative benchmark validations included (i) an instantaneous comparison of the i-τLIF result with that measured by an oxygen microprobe placed at about

Table 3 Photophysical properties of the most common oxygen indicators used in aqueous flow applications

Indicator	Molecular formula	Maximum excitation (nm)	Maximum emission (nm)	Quantum yield (-)	Decay time τ_0 (μs)
PtOEP	$C_{36}H_{44}NPt$	380, 535	650	≈ 0.4	100
PtTFPP	$C_{44}H_8F_{20}N_4Pt$	404, 508	662	≈ 0.4	69
Ru(dpp)	$C_{72}H_{48}Cl_2N_6Ru$	463	618	0.3	6.4
$[Ru(phen)_3]^{2+}$	$C_{36}H_{24}Cl_2N_6Ru.xH_2O$	447	604	0.058	1.0
$[Ru(bpy)]_3]^{2+}$	$C_{30}H_{24}Cl_2N_6Ru{\cdot}6\,H_2O$	452	603	0.042	0.6
PBA	$C_{20}H_{16}O_2$	326, 343	377, 397	–	0.135–0.205

Data taken from: Papkovsky (1993); Vaughan and Weber (1970); Borisov et al. (2008); Quaranta et al. (2012); Papkovsky and Dmitriev (2013)

Abbreviations:

PtOEP = Pt(II) octaethylporphyrin

PtTFPP = Pt(II)mesotetra(pentafluorophenyl)porphyrin

Ru(bpy) = Ru(bipyridine)

Ru(phen) = Dichlorotris-(1,10-phenanthrolin)-ruthenium(II) Hydrat

Ru(dpp)= Ru(4,7'-diphenyl-1,10-phenanthroline)$_3$

PBA = pyrenebutyric acid

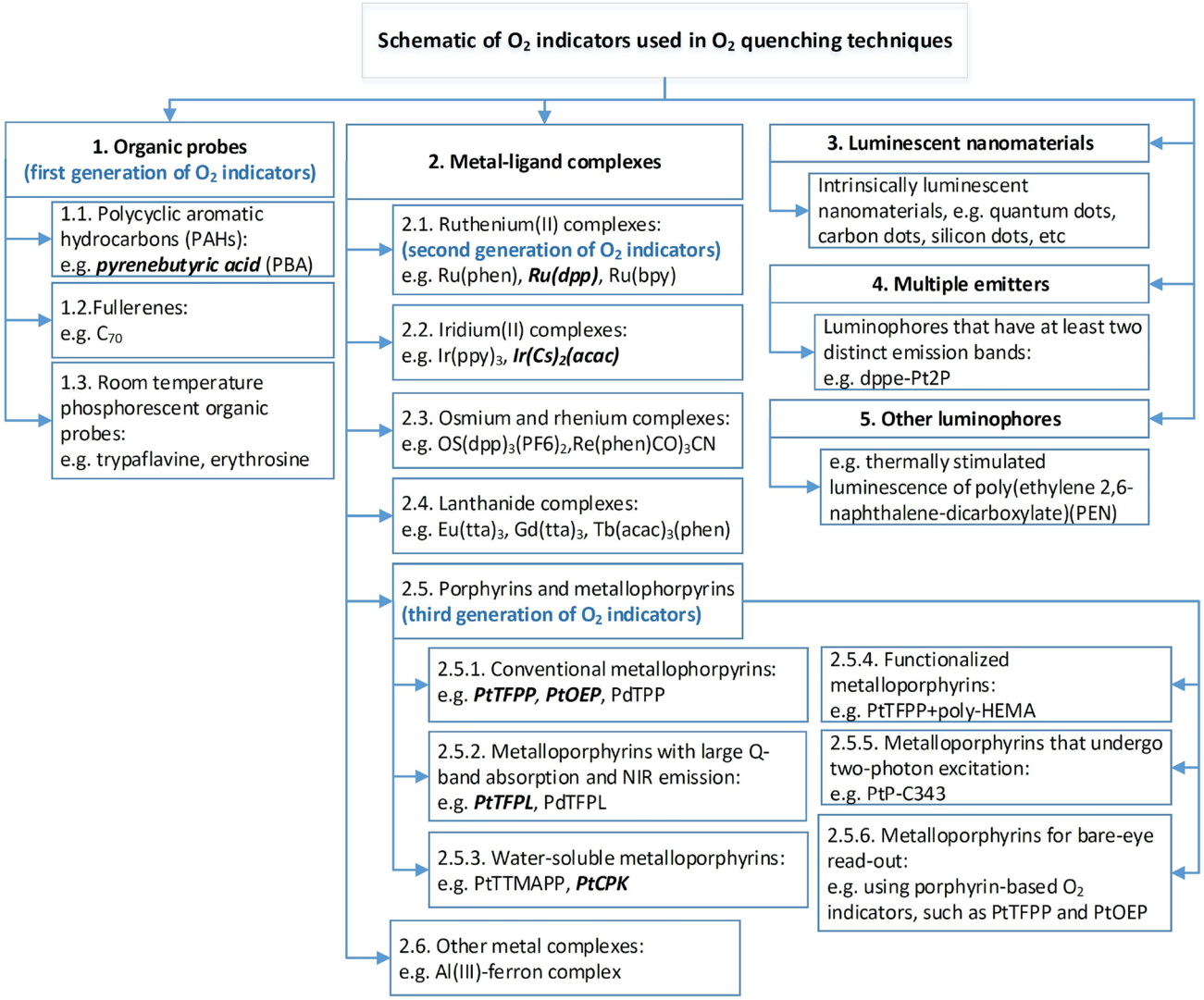

Fig. 18 Schematic of oxygen indicators used in oxygen quenching techniques summarized from Wang and Wolfbeis (2014) and Quaranta et al. (2012). The bold cursive letters indicate the most popular indicators in their respective category. Metalloporphyrins with large Q-band absorption and NIR emission are mostly used for oxygen indicators in fiber-optic sensors, while PtTFPP and PtOEP are mostly used in planar films/optodes and nano-/macroparticles. PBA and Ruthenium complexes are mostly used in LIF applications

0.23 mm below the water surface, (ii) a comparison of the i-τ LIF averaged concentration profile with those measured by an oxygen-probe microprofiler, and (iii) a comparison of the instantaneous transfer velocity k_L quantified directly from the horizontally averaged i-τLIF concentration profiles with the overall K_L determined through longtime bulk concentration measurements. All benchmark validations showed very good agreement proving the reliability of the proposed i-τ LIF approach for studying the gas transfer process near the air–water interface.

Appendix

Acknowledgements This work was financially supported by the German Research Foundation (DFG HE 5609/2-1). We thank Prof. Dr. Andreas Lorke for his valuable input. We also thank Dieter Groß for his assistance in various aspects of the experimental setup.

Funding Open Access funding enabled and organized by Projekt DEAL.

References

Borisov SM, Klimant I (2007) Ultrabright oxygen optodes based on cyclometalated iridium(iii) coumarin complexes. Anal Chem 79(19):7501–7509. https://doi.org/10.1021/ac0710836

Borisov SM, Mayr T, Klimant I (2008) Poly(styrene-block-vinylpyrrolidone) beads as a versatile material for simple fabrication of optical nanosensors. Anal Chem 80(3):573–82. https://doi.org/10.1021/ac071374e

Castellano FN, Lakowicz JR (1998) A water-soluble luminescence oxygen sensor. Photochem Photobiol 67(2):179–183. https://doi.org/10.1111/j.1751-1097.1998.tb05184.x

Chan SP, Fuller ZJ, Demas JN, DeGraff BA (2001) Optimized gating scheme for rapid lifetime determinations of single-exponential luminescence lifetimes. Anal Chem 73(18):4486–4490. https://doi.org/10.1021/ac0102361

Crimaldi JP (2008) Planar laser induced fluorescence in aqueous flows. Exp Fluids 44(6):851–863. https://doi.org/10.1007/s00348-008-0496-2

de Grauw CJ, Gerritsen HC (2001) Multiple time-gate module for fluorescence lifetime imaging. Appl Spectrosc 55(6):670–678. https://doi.org/10.1366/0003702011952587

Digman MA, Caiolfa VR, Zamai M, Gratton E (2008) The phasor approach to fluorescence lifetime imaging analysis. Biophys J 94(2):L14–L16. https://doi.org/10.1529/biophysj.107.120154

Falkenroth A, Degreif K, Jähne B (2007) Visualisation of oxygen concentration fields in the mass boundary layer by fluorescence quenching. Springer, Berlin, pp 59–72

Fereidouni F, Esposito A, Blab GA, Gerritsen HC (2011) A modified phasor approach for analyzing time-gated fluorescence lifetime images. J Microsc 244(3):248–258. https://doi.org/10.1111/j.1365-2818.2011.03533.x

Francois J, Dietrich N, Guiraud P, Cockx A (2011) Direct measurement of mass transfer around a single bubble by micro-Plifi. Chem Eng Sci 66(14):3328–3338. https://doi.org/10.1016/j.ces.2011.01.049

Frederiksen MS, Glud RN (2006) Oxygen dynamics in the rhizosphere of Zostera marina: a two-dimensional planar Optode study. Limnol Oceanogr 51(2):1072–1083. https://doi.org/10.4319/lo.2006.51.2.1072

Friedl F (2013) Investigating the transfer of oxygen at the wavy air-water interface under wind-induced turbulence. University of Heidelberg, Germany, Thesis

Glud RN, Berg P, Stahl H, Hume A, Larsen M, Eyre BD, Cook PLM (2016) Benthic carbon mineralization and nutrient turnover in a Scottish sea loch: an integrative in situ study. Aquat Geochem 22(5):443–467. https://doi.org/10.1007/s10498-016-9300-8

Herlina H, Jirka GH (2004) Application of LIF to investigate gas transfer near the air-water interface in a grid-stirred tank. Exp Fluids 37:341–349. https://doi.org/10.1007/s00348-004-0822-2

Herlina H, Jirka GH (2008) Experiments on gas transfer at the air-water interface induced by oscillating grid turbulence. J Fluid Mech 594:183–208. https://doi.org/10.1017/s0022112007008968

Herlina H, Wissink JG (2019) Simulation of air-water interfacial mass transfer driven by high-intensity isotropic turbulence. J Fluid Mech 860:419–440. https://doi.org/10.1017/jfm.2018.884

Holst G, Kohls O, Klimant I, Konig B, Kuhl M, Richter T (1998) A modular luminescence lifetime imaging system for mapping oxygen distribution in biological samples. Sens Actuat B-Chem 51(1–3):163–170. https://doi.org/10.1016/S0925-4005(98)00232-9

Inglev R, Møller E, Højgaard J, Bang O, Janting J (2021) Optimization of all-polymer optical fiber oxygen sensors with antenna dyes and improved solvent selection using Hansen solubility parameters. Sensors 21(5):1–15. https://doi.org/10.3390/s21010005

Jähne B, Haussecker H (1998) Air-water gas exchange. Ann Rev Fluid Mech 30(1):443–468. https://doi.org/10.1146/annurev.fluid.30.1.443

Jimenez M, Dietrich N, Grace JR, Hebrard G (2014) Oxygen mass transfer and hydrodynamic behaviour in wastewater: determination of local impact of surfactants by visualization techniques. Water Res 58:111–21. https://doi.org/10.1016/j.watres.2014.03.065

Jirka GH, Herlina H, Niepelt A (2010) Gas transfer at the air-water interface: experiments with different turbulence forcing mechanisms. Exp Fluids 49(1):319–327. https://doi.org/10.1007/s00348-010-0874-4

Jähne B (1980) Zur Parametrisierung des Gasaustausches mit Hilfe von Laborexperimente. Universität Heidelberg, Thesis

Kräuter C, Trofimova D, Kiefhaber D, Krah N et al (2014) High resolution 2-D fluorescence imaging of the mass boundary layer thickness at free water surfaces. J Europ Opt Soc Rapid Public 9:14016-1–6. https://doi.org/10.2971/jeos.2014.14016

Kühl M, Polerecky L (2008) Functional and structural imaging of phototrophic microbial communities and symbioses. Aquat Microb Ecol 53:99–118. https://doi.org/10.3354/ame01224

Lakowicz JR (2010) *Time-Domain Lifetime Measurements*, Book section Chapter 4, pp. 97–155. Boston, MA: Springer US

Larsen M, Borisov SM, Grunwald B, Klimant I, Glud RN (2011) A simple and inexpensive high resolution color ratiometric planar optode imaging approach: application to oxygen and ph sensing. Limnol Oceanogr Methods 9(9):348–360. https://doi.org/10.4319/lom.2011.9.348

Lebrun G, Xu F, Le Men C, Hébrard G, Dietrich N (2021) Gas-liquid mass transfer around a rising bubble: combined effect of rheology and surfactant. Fluids 6(2):84. https://doi.org/10.3390/fluids6020084

Lee SK, Okura I (1997) Photostable optical oxygen sensing material: platinum tetrakis(pentafluorophenyl)porphyrin immobilized in polystyrene. Anal Commun 34(6):185–188. https://doi.org/10.1039/a701130j

Liebsch G, Klimant I, Frank B, Holst G, Wolfbeis OS (2000) Luminescence lifetime imaging of oxygen, ph, and carbon dioxide distribution using optical sensors. Appl Spectrosc 54(4):548–559. https://doi.org/10.1366/0003702001949726

Liss PS (1973) Processes of gas exchange across an air-water interface. Deep-Sea Res Oceanogr Abstr 20(3):221–238. https://doi.org/10.1016/0011-7471(73)90013-2

Lo LW, Koch CJ, Wilson DF (1996) Calibration of oxygen-dependent quenching of the phosphorescence of pd-meso-tetra (4-carboxyphenyl) porphine: a phosphor with general application for measuring oxygen concentration in biological systems. Anal Biochem 236(1):153–160. https://doi.org/10.1006/abio.1996.0144

Ma X, Sun R, Cheng J, Liu J, Gou F, Xiang H, Zhou X (2016) Fluorescence aggregation-caused quenching versus aggregation-induced emission: a visual teaching technology for undergraduate chemistry students. J Chem Educ 93(2):345–350. https://doi.org/10.1021/acs.jchemed.5b00483

Malacrida L, Ranjit S, Jameson DM, Gratton E (2021) The phasor plot: a universal circle to advance fluorescence lifetime analysis and interpretation. Ann Rev Biophys 50:575–593. https://doi.org/10.1146/annurev-biophys-062920-063631

Mayr T, Borisov SM, Abel T, Enko B, Waich K, Mistlberger G, Klimant I (2009) Light harvesting as a simple and versatile way to enhance brightness of luminescent sensors. Anal Chem 81(15):6541–6545. https://doi.org/10.1021/ac900662x

Mosshammer M, Brodersen KE, Kuhl M, Koren K (2019) Nanoparticle- and microparticle-based luminescence imaging of chemical species and temperature in aquatic systems: a review. Mikrochim Acta 186(2):126. https://doi.org/10.1007/s00604-018-3202-y

Münsterer T (1996) November. *LIF Investigation of the mechanisms controlling air-water mass transfer at a free interface*. Ph. D. thesis, Faculty for Physics and Astronomy, Heidelberg University

Murniati E, Gross D, Herlina H, Hancke K, Glud RN, Lorke A (2016) Oxygen imaging at the sediment-water interface using lifetime-based laser induced fluorescence (τLIF) of nano-sized particles. Limnol Oceanogr Methods 14(8):506–517. https://doi.org/10.1002/lom3.10108

Murniati E, Gross D, Herlina H, Hancke K, Lorke A (2017) Effects of bioirrigation on the spatial and temporal dynamics of oxygen above the sediment-water interface. Freshwater Sci 36(4):784–795. https://doi.org/10.1086/694854

Nagel L, Krall KE, Jähne B (2015) Comparative heat and gas exchange measurements in the Heidelberg Aeolotron, a large annular wind-wave tank. Ocean Sci 11(1):111–120. https://doi.org/10.5194/os-11-111-2015

Papkovsky DB (1993) Luminescent porphyrins as probes for optical (bio)sensors. Sens Actuat B Chem 11(1):293–300. https://doi.org/10.1016/0925-4005(93)85267-E

Papkovsky DB (2004) Methods in optical oxygen sensing: protocols and critical analyses, vol 381. Academic Press, Cambridge, pp 715–735

Papkovsky DB, Dmitriev RI (2013) Biological detection by optical oxygen sensing. Chem Soc Rev 42(22):8700–32. https://doi.org/10.1039/c3cs60131e

Pinelli M, Herlina H, Wissink JG, Uhlmann M (2022) Direct numerical simulation of turbulent mass transfer at the surface of an open channel flow. J Fluid Mech 933:A49. https://doi.org/10.1017/jfm.2021.1080

Quaranta M, Borisov SM, Klimant I (2012) Indicators for optical oxygen sensors. Bioanal Rev 4(2):115–157. https://doi.org/10.1007/s12566-012-0032-y

Roudet M, Billet AM, Cazin S, Risso F, Roig V (2017) Experimental investigation of interfacial mass transfer mechanisms for a confined high-Reynolds-number bubble rising in a thin gap. AIChE J 63(6):2394–2408. https://doi.org/10.1002/aic.15562

Rüttinger S, Spille C, Hoffmann M, Schlüter M (2018) Laser-induced fluorescence in multiphase systems. Chem Bio Eng Rev 5(4):253–269. https://doi.org/10.1002/cben.201800005

Rysgaard S, Glud RN, Sejr MK, Blicher ME, Stahl HJ (2008) Denitrification activity and oxygen dynamics in arctic sea ice. Polar Biol 31(5):527–537. https://doi.org/10.1007/s00300-007-0384-x

Santner J, Larsen M, Kreuzeder A, Glud RN (2015) Two decades of chemical imaging of solutes in sediments and soils-a review. Anal Chim Acta 878:9–42. https://doi.org/10.1016/j.aca.2015.02.006

Schladow SG, Lee M, Hurzeler BE, Kelly PB (2002) Oxygen transfer across the air-water interface by natural convection in lakes. Limnol Oceanogr 47(5):1394–1404. https://doi.org/10.4319/lo.2002.47.5.1394

Soloviev A, Lukas R (2014) The near-surface layer of the ocean Structure. Dynamics and Applications. Cambridge, Cambridge

Takagaki N, Kurose R, Kimura A, Komori S (2016) Effect of schmidt number on mass transfer across a sheared gas-liquid interface in a wind-driven turbulence. Sci Rep 6(1):37059. https://doi.org/10.1038/srep37059

Vaughan WM, Weber G (1970) Oxygen quenching of pyrenebutyric acid fluorescence in water. a dynamic probe of the microenvironment. Biochemistry 9(3):464–73. https://doi.org/10.1021/bi00805a003

Wang XD, Wolfbeis OS (2014) Optical methods for sensing and imaging oxygen: materials, spectroscopies and applications. Chem Soc Rev 43(10):3666–761. https://doi.org/10.1039/c4cs00039k

Wissink JG, Herlina H (2016) Direct numerical simulation of gas transfer across the air-water interface driven by buoyant convection. J Fluid Mech 787:508–540. https://doi.org/10.1017/jfm.2015.696

Wissink JG, Herlina H (2023) Surface-temperature-induced marangoni effects on developing buoyancy-driven flow. J Fluid Mech 962:A23. https://doi.org/10.1017/jfm.2023.263

Wissink JG, Herlina H, Akar Y, Uhlmann M (2017) Effect of surface contamination on interfacial mass transfer rate. J Fluid Mech 830:5–34. https://doi.org/10.1017/jfm.2017.566

Wolfbeis OS (2015) Luminescent sensing and imaging of oxygen: Fierce competition to the clark electrode. BioEssays 37(8):921–928. https://doi.org/10.1002/bies.201500002

Wolfbeis OS (2015) An overview of nanoparticles commonly used in fluorescent bioimaging. Chem Soc Rev 44(14):4743–68. https://doi.org/10.1039/c4cs00392f

Zhang Q, Handler RA, Fredriksson ST (2013) Direct numerical simulation of turbulent free convection in the presence of a surfactant. Int J Heat Mass Transf 61:82–93. https://doi.org/10.1016/j.ijheatmasstransfer.2013.01.031

Authors and Affiliations

E. Murniati[1] · A. Philippe[2] · O. Eiff[1] · H. Herlina[1]

✉ H. Herlina
herlina.herlina@kit.edu

E. Murniati
erni.murniati@kit.edu

A. Philippe
a.philippe@rptu.de

O. Eiff
olivier.eiff@kit.edu

[1] Institute for Water and Environment, Karlsruhe Institute of Technology, Kaiserstrasse 12, 76131 Karlsruhe, Baden-Wuerttemberg, Germany

[2] iES Landau - Institute for Environmental Sciences, University of Kaiserslautern-Landau (RPTU), Fortstrasse 7, 76829 Landau, Rheinland-Pfalz, Germany